Supporting information

Structural flexibility in cationic metal-organic framework for boosting ReO_4^- capture

Shufen Gu,[a] Zhiwu Yu,[b] Ning Li,[2] Qingyun Zhang,[a] Huiping Zhang,[a] Lipeng Zhang,[c] Lele Gong,[c] Rajamani Krishna[d] and Feng Luo[a]*

Correponding author: F. L. ecitluofeng@163.com

X-ray Crystallography

X-ray diffraction data were collected on a Bruker diffractometer. The data reduction included a correction for Lorentz and polarization effects, with an applied multiscan absorption correction (SADABS). The crystal structure was solved and refined using the SHELXTL program suite. Direct methods yielded all non-hydrogen atoms, which were refined with anisotropic thermal parameters. All hydrogen atom positions were calculated geometrically and were riding on their respective atoms. The SQUEEZE subroutine of the PLATON software suite was used to remove the scattering from the highly disordered guest molecules. CCDC 2201226-2201231 contains the supplementary crystallographic data of these materials, respectively. These data can be obtained free of charge from the Cambridge Crystallographic Data Centre via www.ccdc.cam.ac.uk/ data_request/cif.

Experiment for the sorption of ReO_4^-: The starting Re stock solution was made by dissolving 1.44 g NH_4ReO_4 in 1000 mL deionized water to create an 1000 mg/L (ppm) NH_4ReO_4 solution. All the adsorption experiments were conducted at 298 K.

In the sorption kinetics experiment, ReO_4^- solution with initial concentration of 65 ppm was used. The dose of adsorbent is 10 mg, while volume of ReO_4^- solution is 30 mL.

In the sorption isotherm experiment, ReO_4^- solution with initial concentration of 100-700 ppm was used. The dose of adsorbent is 10 mg, while the volume of ReO_4^- solution is 20 mL and the contact time is 5 h.

The adsorption amount, q(mg/g), was calculated by the difference of the ReO_4^- equilibrium concentration before and after adsorption (equation 1), where C_0, and C_e are the initial and equilibrium concentration of ReO_4^-, V is the volume of solution, m is the mass of used sample.

$$q = \frac{(C_0 - C_e) \times V}{m} \quad (1)$$

In the selective adsorption experiments, KNO_3, K_2CO_3, K_3PO_4, $KClO_4$ or K_2SO_4 was used to generate the mixed ion solution containing 125 ppm ReO_4^- and other ions (125 ppm) such as NO_3^-,

or CO_3^{2-}, or PO_4^{3-}, or ClO_4^- , or SO_4^{2-}. The dose of adsorbent is 10 mg, while the volume of mixed ion solution is 20 mL and the contact time is 5 h.

The K_d value was determined with adsorbent of 10 mg, volume of 30 mL, ReO_4^- concentration of 1 ppm, contact time of 24 h, temprature at 298 K.

In the recycle experiments, the first adsorption was carried out with adsorbent of 10 mg, volume of 20 mL, ReO_4^- concentration of 65 ppm, contact time of 5 h, temprature at 298 K. Then the desorption was achieved by soaking ReO_4^- loaded samples in 3 M $NaNO_3$ solution (30 mL, adsorbents with NO_3^- as counterion) or 3M NaCl solution (30 mL, adsorbents with Cl^- as counterion). Then the second adsorption experiment was carried out based on the desorbed samples, except for **Co-TIB-NO_3-313** and **Co-TIB-Cl-313** adsorbents that request further redegassing under vacuum at 313 K for 24 h.

For all the adsorption test, the errors is about 3%.

The sorption data fitting by isotherm models

The Langmuir model assumes that the sorption of metal ions occurs on a homogenous surface by monolayer sorption and there no interaction between adsorbed ions, with homogeneous binding sites and equivalent sorption energies. The linear equation of the Langmuir isotherm model is expressed as followed:

$$\frac{C_e}{q_e} = \frac{1}{q_m k_L} + \frac{C_e}{q_m} \qquad (2)$$

where q_m is the maximum sorption capacity corresponding to complete monolayer coverage (mg/g) and k_L is a constant indirectly related to sorption capacity and energy of sorption (L/mg), which characterizes the affinity of the adsorbate with the adsorbent. The linearized plot was obtained when we plotted C_e/q_e against Ce and q_m and k_L could be calculated from the slope and intercept (Table S1).

The Freundlich equation is an empirical equation based on sorption on a heterogeneous surface. The isotherm assumes that adsorbent surface sites have a spectrum of different binding energies.

The linear equation can be expressed by:

$$Ln\,q_e = Ln\,k_F + \frac{1}{n} Ln\,C_e \quad (3)$$

where k_F and n are the Freundlich constants related to the sorption capacity and the sorption intensity, respectively.

The adsorption kinetics was analyzed by simplified kinetic models such as the pseudo-first-order and pseudo-second-order, through the following two equations:

$$Ln(q_e - q_t) = Ln\,q_e - k_1 \quad (4)$$

$$\frac{t}{q_t} = \frac{1}{k_2 \times q_e^2} + \frac{t}{q_e} \quad (5)$$

Where q_e (mg/g) and q_t (mg/g) are the quantity of the adsorbed ReO_4^- at equilibrium and at t time, respectively, and $k_1(min^{-1})/k_2[g/(mg \cdot min)]$ is the pseudo-first/second-order sorption rate constant that is deduced from the slope of the plot of t/q_t versus t (Table S2).

The K_d value is calculated from the following equation,

$$K_d = \frac{V}{m} \frac{C_0 - C_e}{C_e} \quad (6)$$

Computational Methods

The first-principle calculations were performed within the framework of density functional theory (DFT) as implemented in the plane wave set Vienna *Ab-initio* Simulation Package (VASP) code[1-2], in which the Perdew-Burke-Ernzenhof (GGA-PBE) functionalization and the project-augmented wave generalized gradient approximation pseudopotentials (PAW-GGA) were employed to calculate the exchange-correlation energy and electron-ion interaction[3-4], respectively. Additionally, spin-polarization was considered in all calculations.[5] Wave functions were expanded using a plane-wave basis set with kinetic energy cutoff of 500 eV and the geometries were fully relaxed until the residual force convergence value on each atom being less 0.02 eV $Å^{-1}$.[6] A gamma k-point mesh of 1×1×1 for the Brillouin zone sampling for structural optimization. During the

calculations, the periodicity of MOF was maintained for simplicity and saving computational resources.

The detail of calculation of exchange energy (ΔG_a) was listed as follows. The formula of average exchange energy (ΔG_a) was defined:

$$\Delta G_a = \left[G_{\mathrm{MOF@ReO_4^-}} - G_{\mathrm{MOF@Cl^-/NO_3^-}} - 2 \times G_{\mathrm{ReO_4^-}} + 2 \times G_{\mathrm{Cl^-/NO_3^-}}\right]/2$$

Where the $G_{\mathrm{MOF@ReO_4^-}}$ and $G_{\mathrm{MOF@Cl^-/NO_3^-}}$ were the calculation total energy of the MOFs structure with $\mathrm{ReO_4^-}$, $\mathrm{Cl^-}$ or $\mathrm{NO_3^-}$ counterions. The $G_{\mathrm{ReO_4^-}}$, $G_{\mathrm{Cl^-/NO_3^-}}$ and $G_{\mathrm{NO_3^-}}$ were defaulted as the energy of freeous $\mathrm{ReO_4^-}$, $\mathrm{Cl^-}$ or $\mathrm{NO_3^-}$ ions.

[1]. G. Kresse, J. Furthmüller, *Phys. Rev. B*, 1996, 54, 11169.

[2]. G. Kresse, J. Furthmüller, *Comput. Mater. Sci.*, 1996, 6, 15.

[3]. J. P. Perdew, K. Burke, M. Ernzerhof, *Phys. Rev. Lett.*, 1996, 77, 3865.

[4]. I. V. Solvyev, P. H. Dederichs, V. I. Anisimov, *Phys. Rev. B*, 1994, 50, 16861.

[5]. L. Gong, X. Wang, T. Zheng, J. Liu, J. Wang, Y.-C. Yang, J. Zhang, X. Han, L. Zhang, Z. Xia, *J. Mater. Chem. A*, 2021, 9, 3555–3566.

[6]. L. Gong, D. Zhang, C.-Y. Lin, Y. Zhu, Y. Shen, J. Zhang X. Han, L. Zhang, Z. Xia, *Adv. Energy Mater.*, 2019, 9, 1902625.

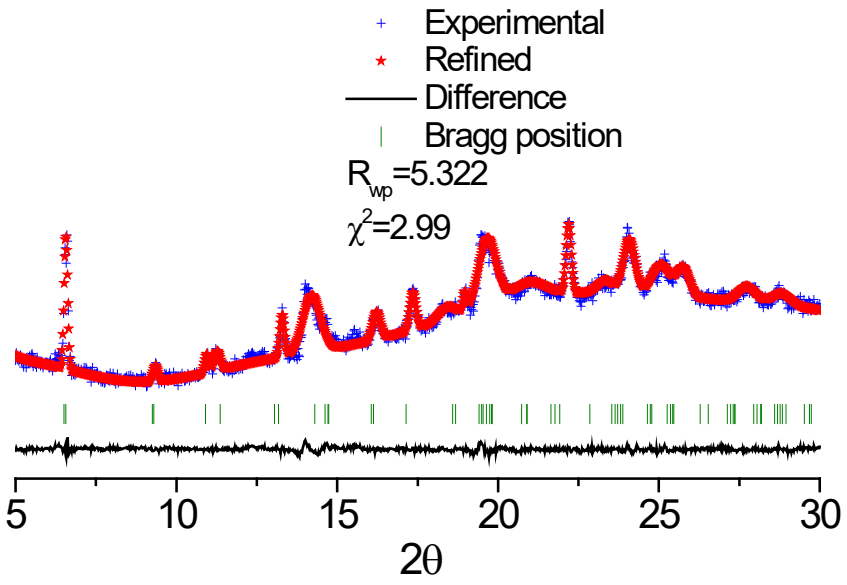

Fig. S1 A comparison between PXRD pattern of as-synthesized samples of **Co-TIB-NO$_3$** and PXRD pattern simulated from single crystal data. The refinement is using GSAS-II program.

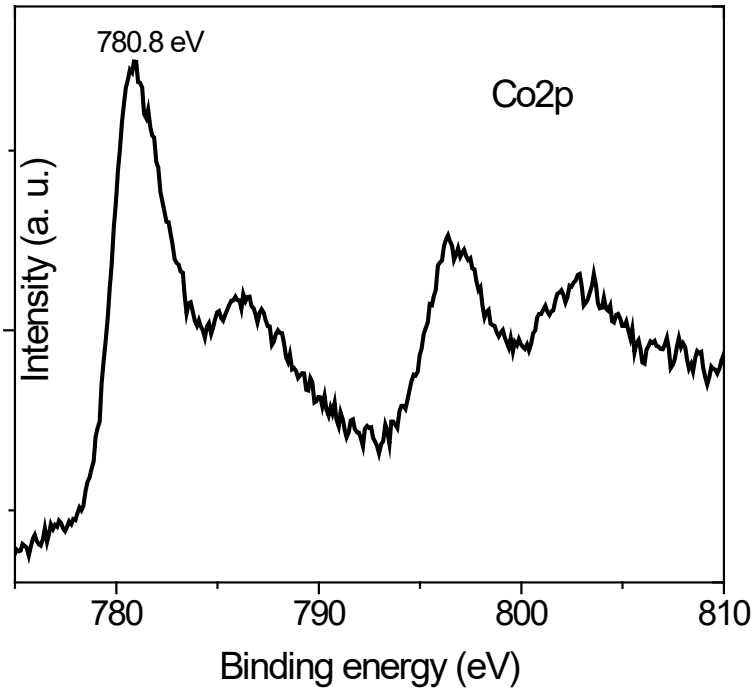

Fig. S2 The XPS of Co element in **Co-TIB-NO_3**. The binding energy of 780.8 eV is comparable with $Co(OH)_2$, suggesting +2 valence of Co(II) in this MOF.

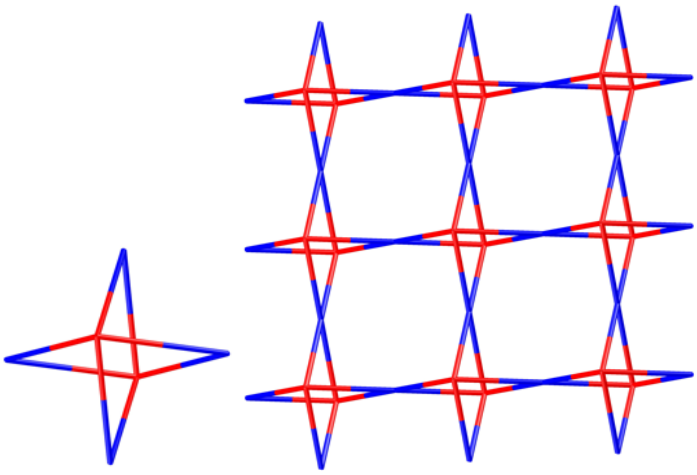

Fig. S3 View of the topology of $Co_2(TIB)_4$ cage and $Co_2(TIB)_4$ cage based double layer.

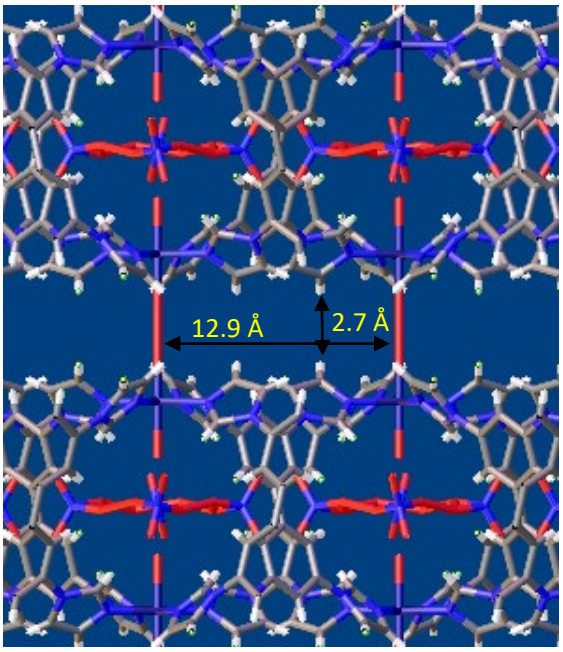

Fig. S4 View of the narrow channel in **Co-TIB-NO_3** along *a* or *b* direction.

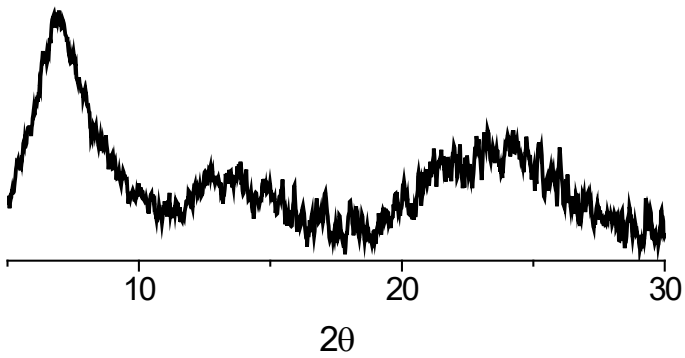

Fig. S5 The PXRD patterns of **Co-TIB-NO_3-313**. The broad diffuse scattering implies non-crystalline state of the resultant samples.

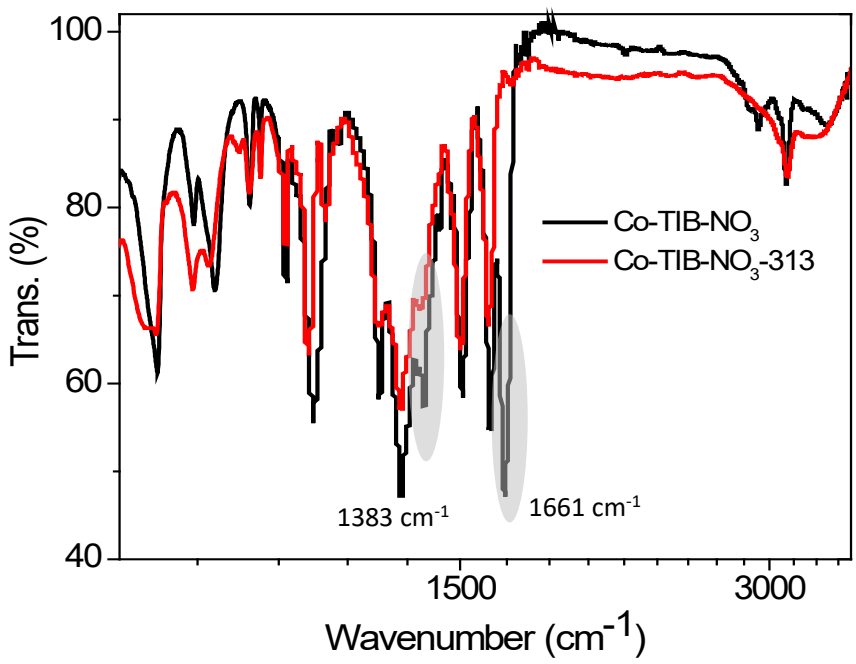

Fig. S6 A comparison of IR between **Co-TIB-NO3** and **Co-TIB-NO3-313**. It is found that the 1383 cm^{-1} peak belonging to NO_3^- is retained, while 1661 cm^{-1} belonging to $(NO_3^-)_4$ tetramer disappeared, indicative of dynamic behavior of $(NO_3^-)_4$ tetramer.

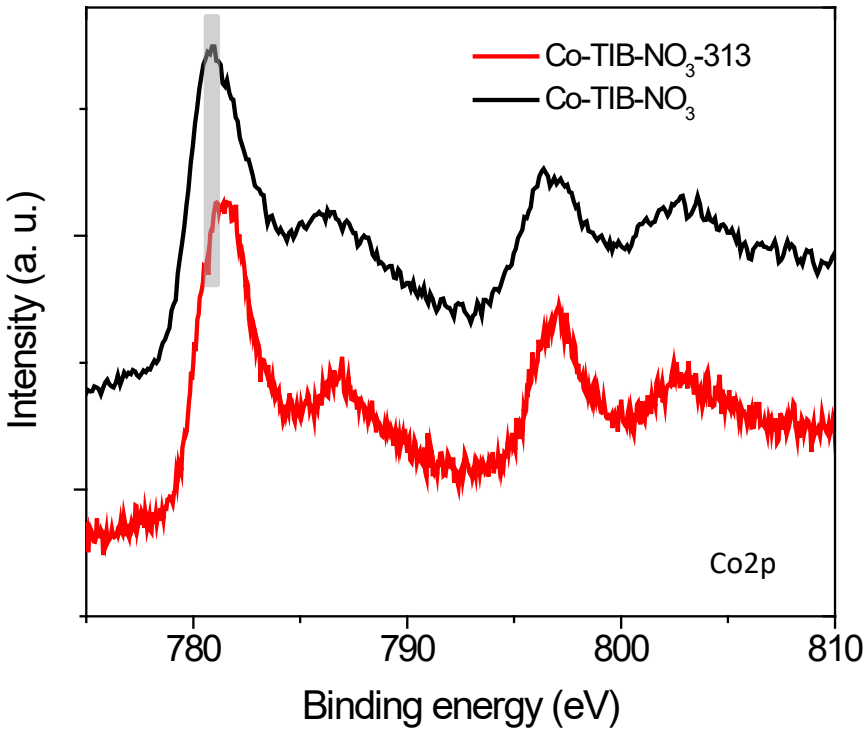

Fig. S7 A comparison of XPS of Co element between **Co-TIB-NO$_3$** and **Co-TIB-NO$_3$-313**. It is clear that Co in **Co-TIB-NO$_3$-313** shifts to higher binding energy, most likely due to interlayer compression that reinforces the additional Co-O coordination bond on the pristine pyramidal geometry.

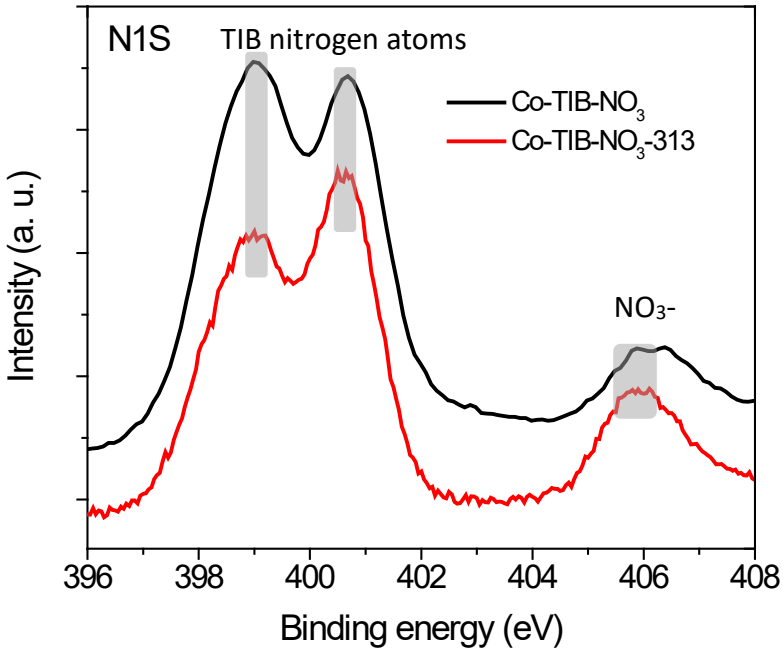

Fig. S8 A comparison of XPS of N element between **Co-TIB-NO$_3$** and **Co-TIB-NO$_3$-313**. It is clear that NO_3^- in **Co-TIB-NO$_3$-313** shifts to lower binding energy, indicative of dynamic behavior of $(NO_3^-)_4$ tetramer.

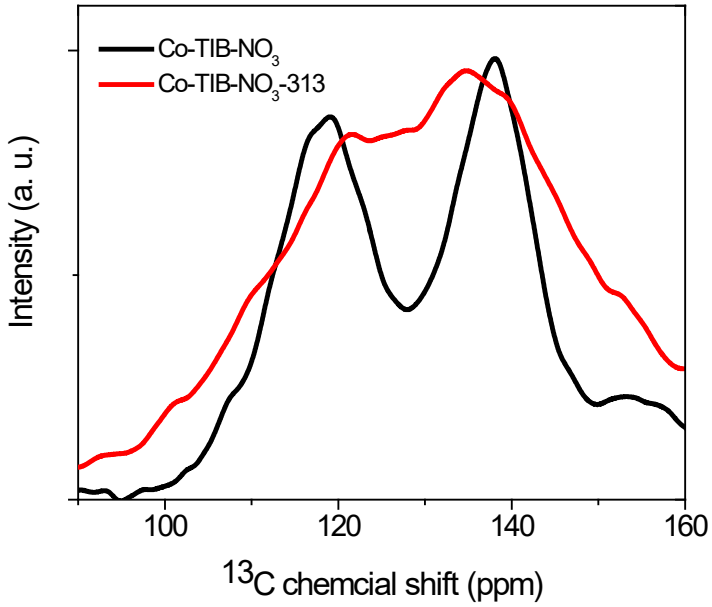

Fig. S9 A comparison of ^{13}C MAS NMR spectra between **Co-TIB-NO$_3$** and **Co-TIB-NO$_3$-313**. The broadened signals of the TIB carbon atoms suggest the disordered skeleton structure in **Co-TIB-NO$_3$-313**.

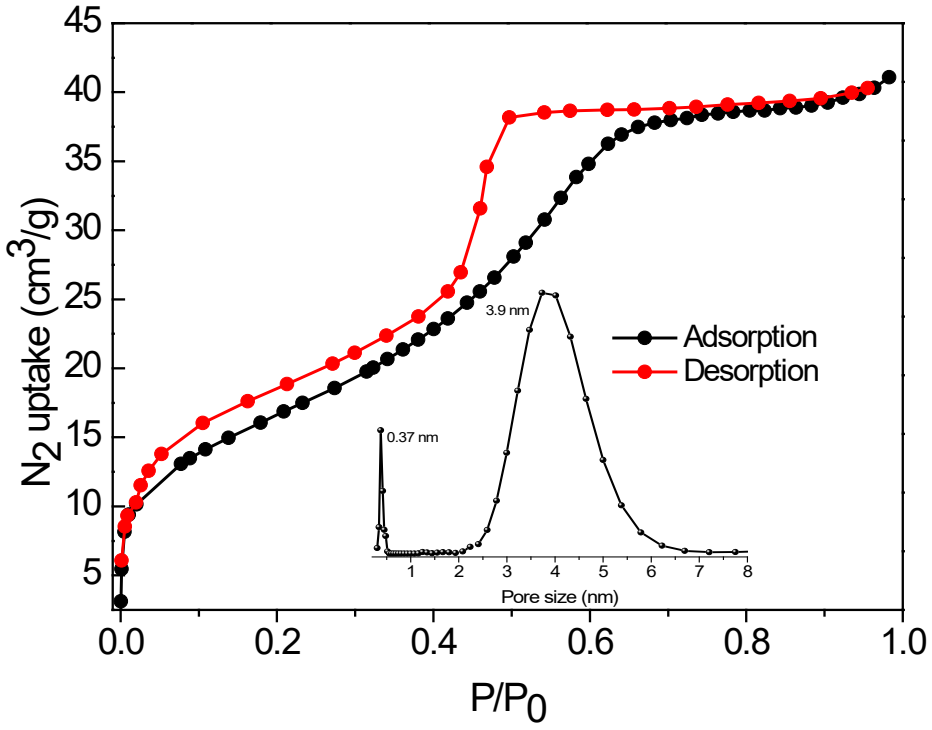

Fig. S10 The N_2 adsorption isotherm at 77 K for **Co-TIB-NO$_3$-313** with the inset of poree size distribution.

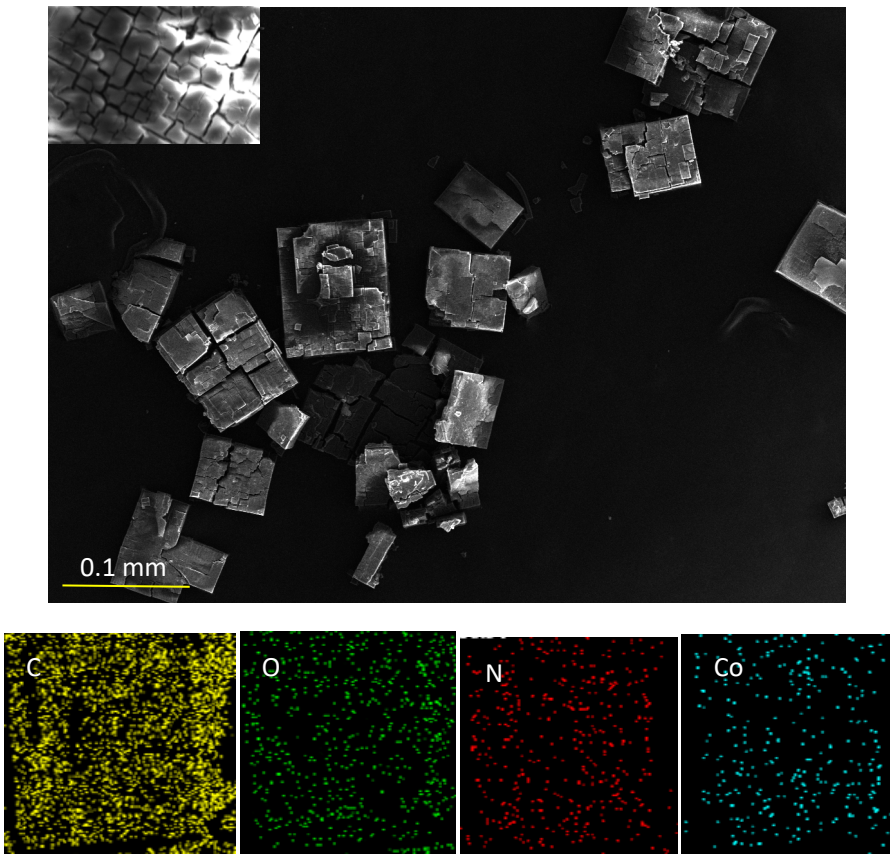

Fig. S11 The SEM images of **Co-TIB-NO_3-313**, where crackles were clearly observed (insert). The EDS mapping shows somewhat uneven distribution of C, O, N, and Co element, due to the disordered structure in **Co-TIB-NO_3-313**.

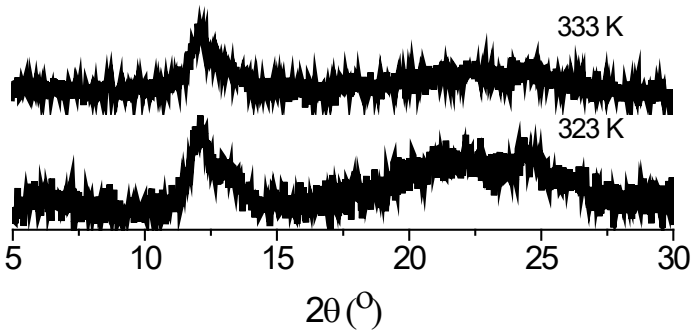

Fig. S12 The PXRD patterns of **Co-TIB-NO$_3$** samples after calcination at 323 K and 333 K for 24 h.

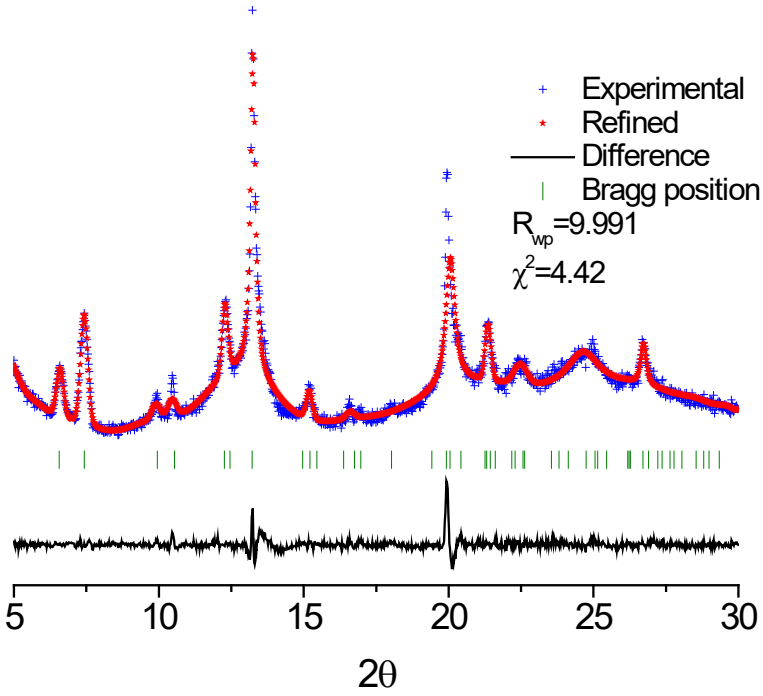

Fig. S13 A comparison between PXRD pattern of **Co-TIB-Cl-313** and PXRD pattern simulated from single crystal data. The refinement is using GSAS-II program.

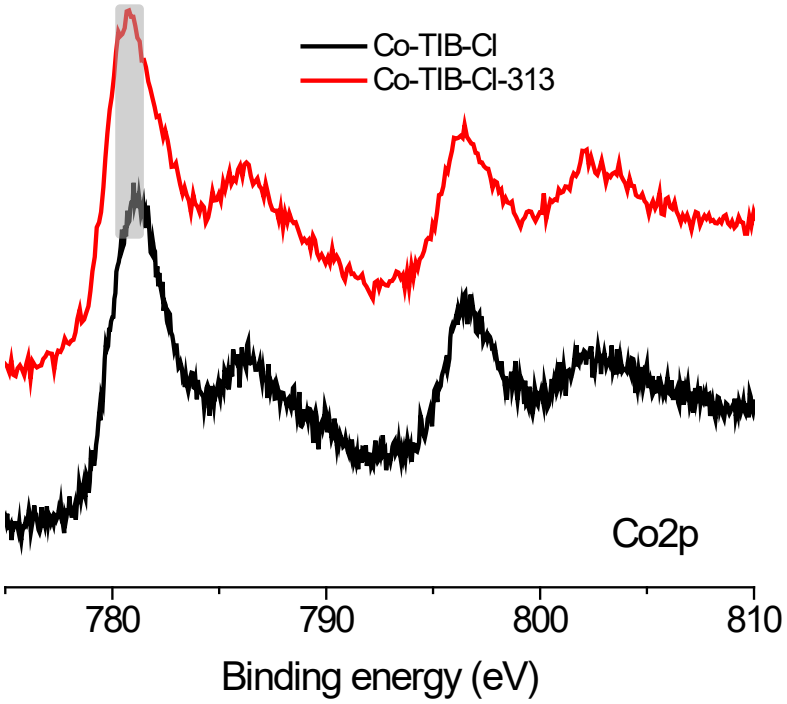

Fig. S14 A comparison of XPS of Co element between **Co-TIB-Cl** and **Co-TIB-Cl-313**, where no detectable change is observed.

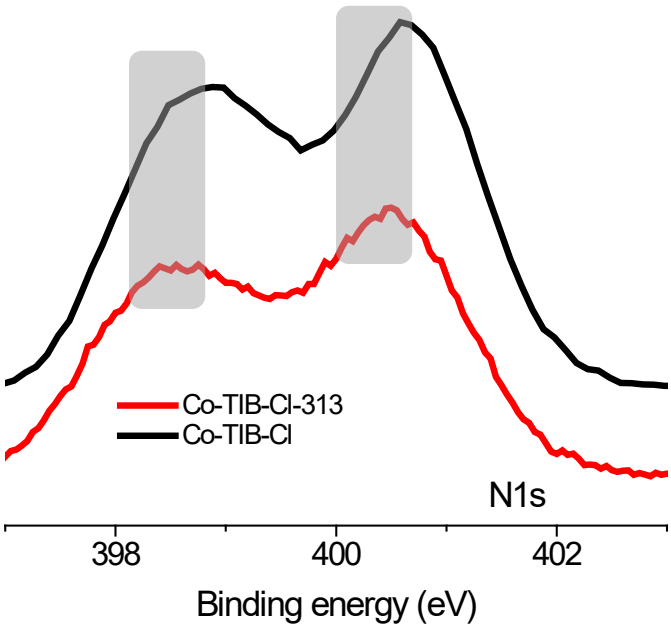

Fig. S15 A comparison of XPS of N element between **Co-TIB-Cl** and **Co-TIB-Cl-313**, where the change suggests the dynamic behavior of TIB ligand.

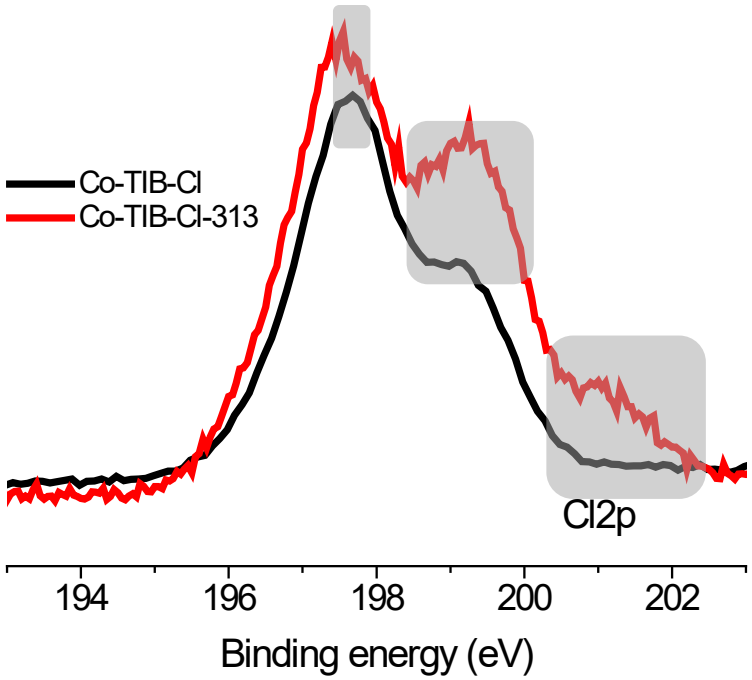

Fig. S16 A comparison of XPS of Cl element between **Co-TIB-Cl** and **Co-TIB-Cl-313**, where the change suggests the dynamic behavior of Cl^- ions.

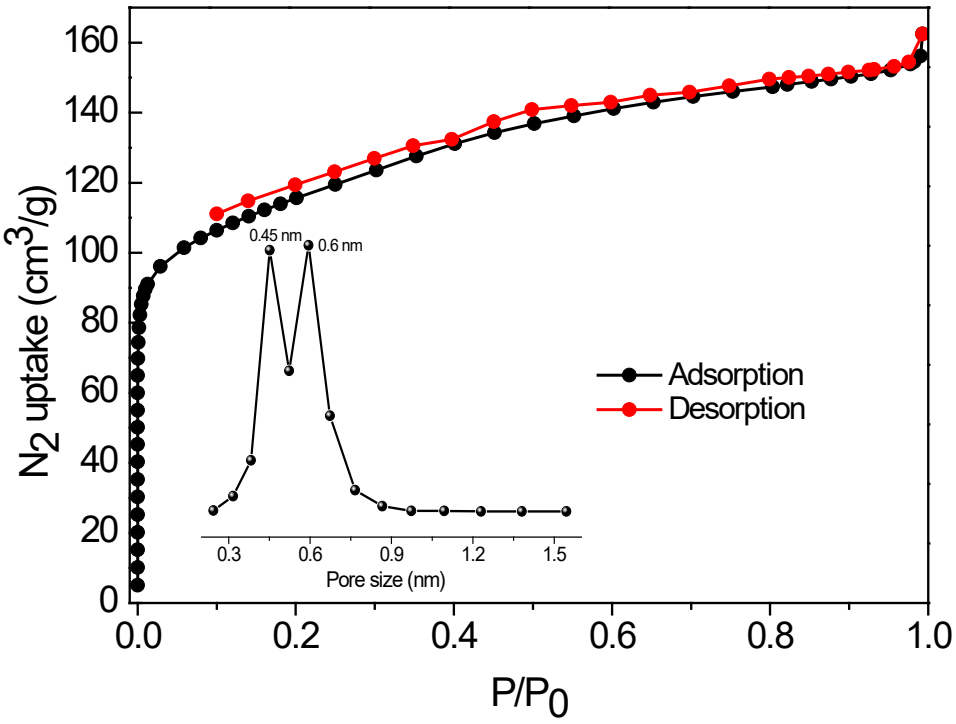

Fig. S17 The N_2 adsorption isotherm at 77 K for **Co-TIB-Cl-313** with the inset of poree size distribution.

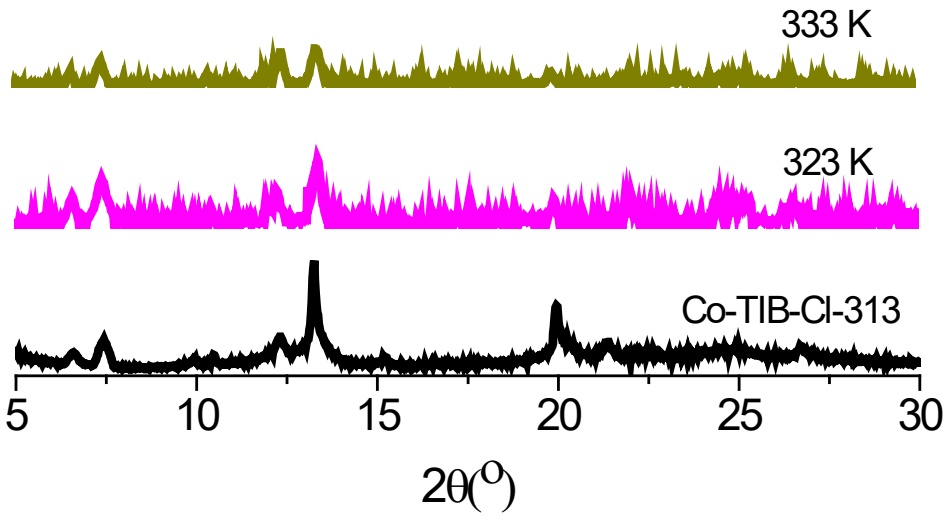

Fig. S18 The PXRD patterns of **Co-TIB-Cl** samples after calcination at 323 K and 333 K for 24 h.

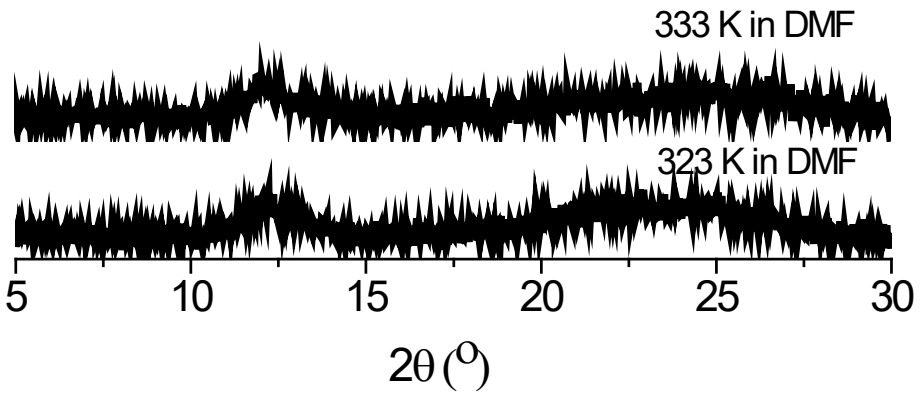

Fig. S19 The recovery of **Co-TIB-NO$_3$** samples after calcination at 323 K and 333 K for 24 h in DMF, traced by PXRD.

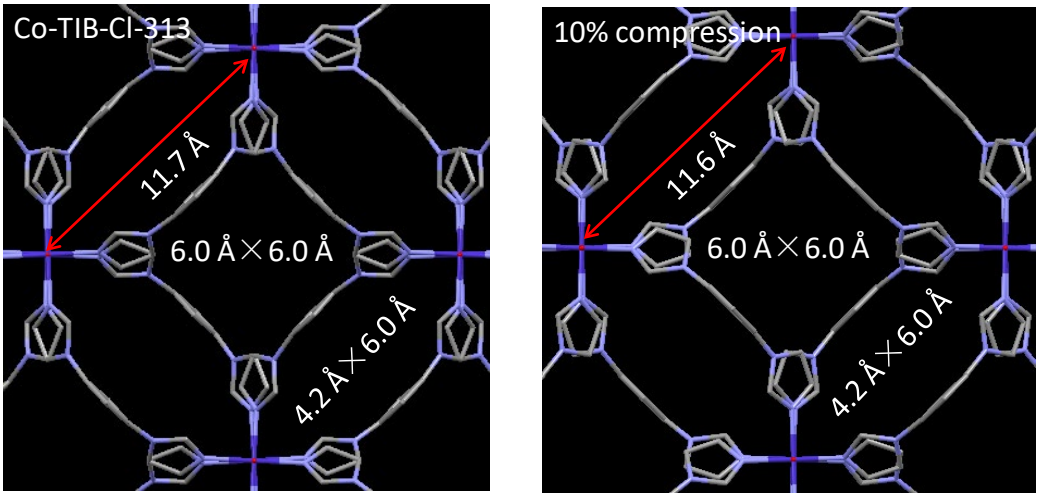

Fig. S20 A comparison of Co-TIB-Cl-313 and the calculated Co-TIB structure under 10% compression.

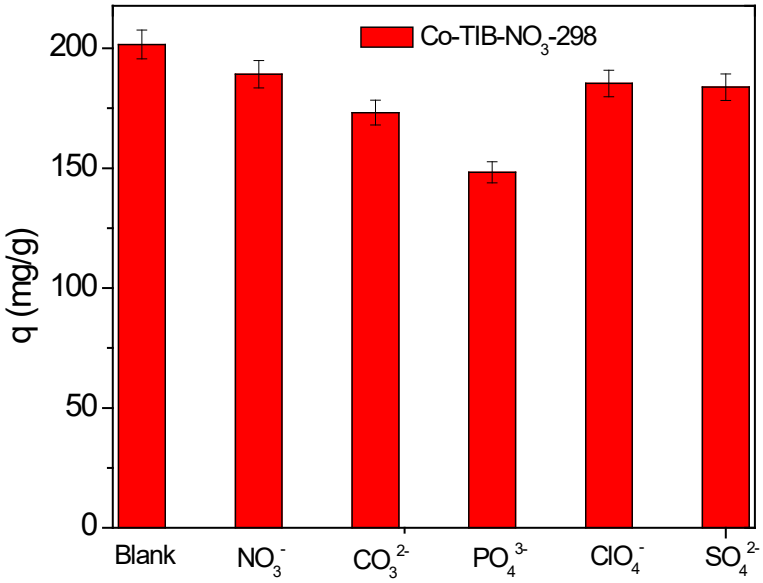

Fig. S21 Effect of competing anions on the ReO_4^- uptake by **Co-TIB-NO3**.

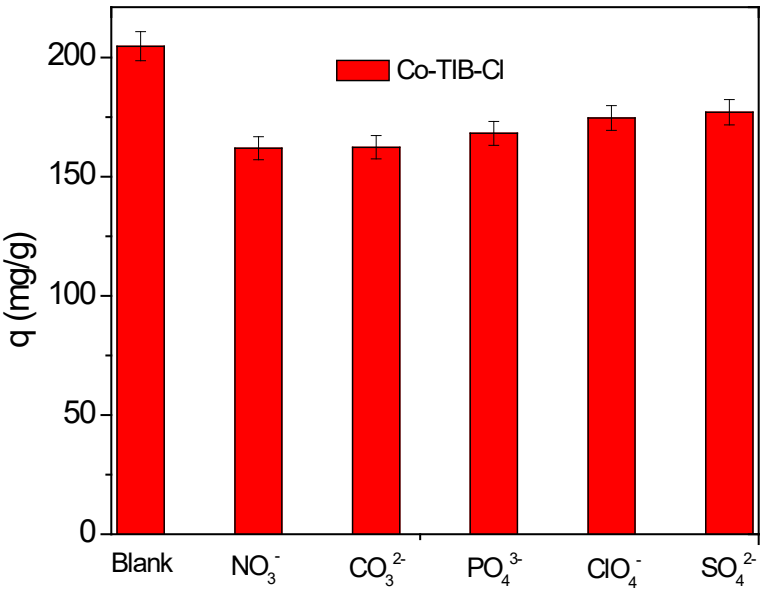

Fig. S22 Effect of competing anions on the ReO_4^- uptake by **Co-TIB-Cl**.

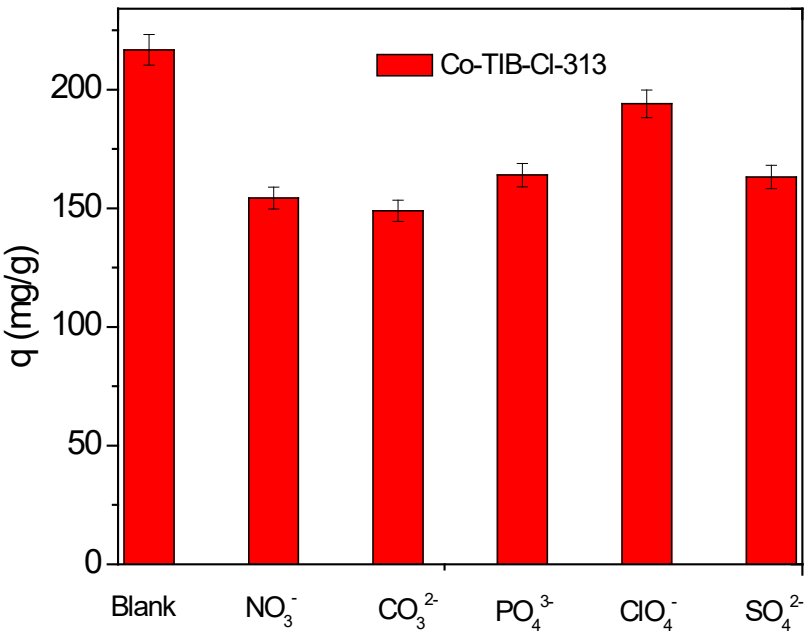

Fig. S23 Effect of competing anions on the ReO_4^- uptake by **Co-TIB-Cl-313**.

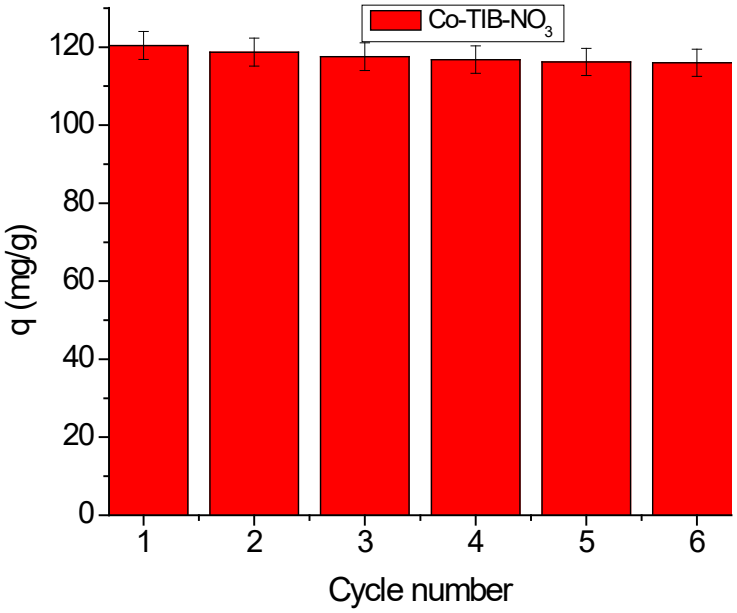

Fig. S24 Recycle use of adsorbent of **Co-TIB-NO3** for ReO_4^- uptake.

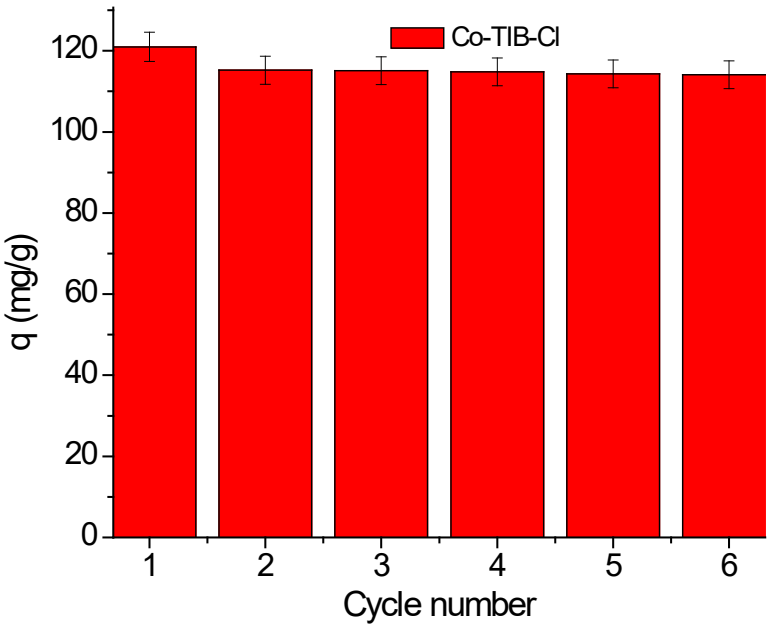

Fig. S25 Recycle use of adsorbent of **Co-TIB-Cl** for ReO_4^- uptake.

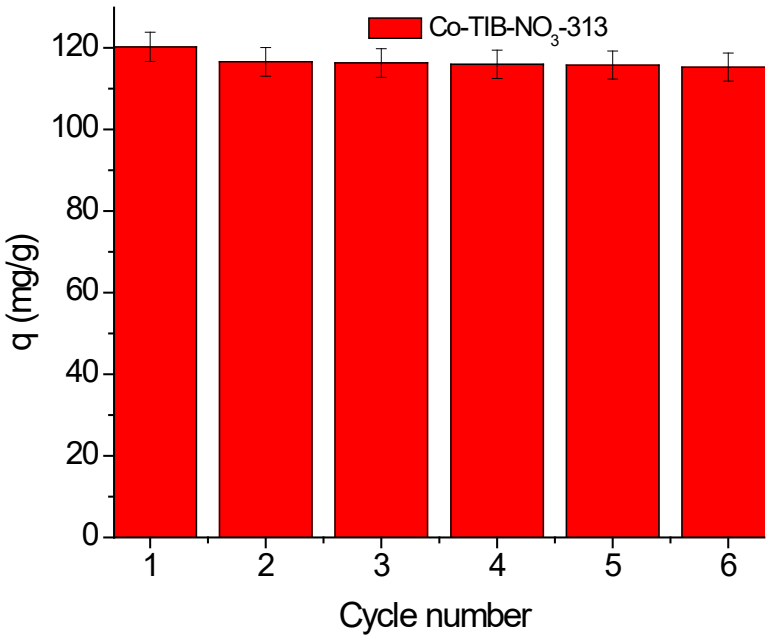

Fig. S26 Recycle use of adsorbent of **Co-TIB-NO3-313** for ReO_4^- uptake.

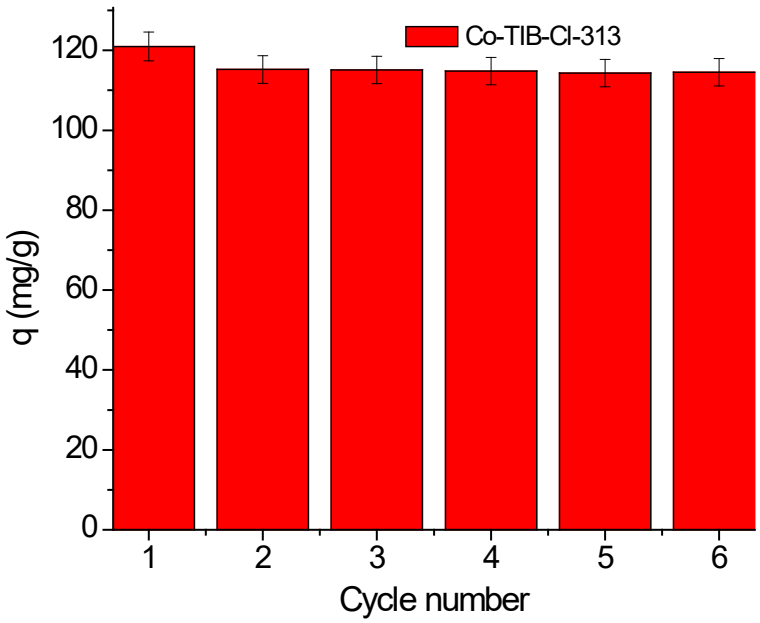

Fig. S27 Recycle use of adsorbent of **Co-TIB-Cl-313** for ReO_4^- uptake.

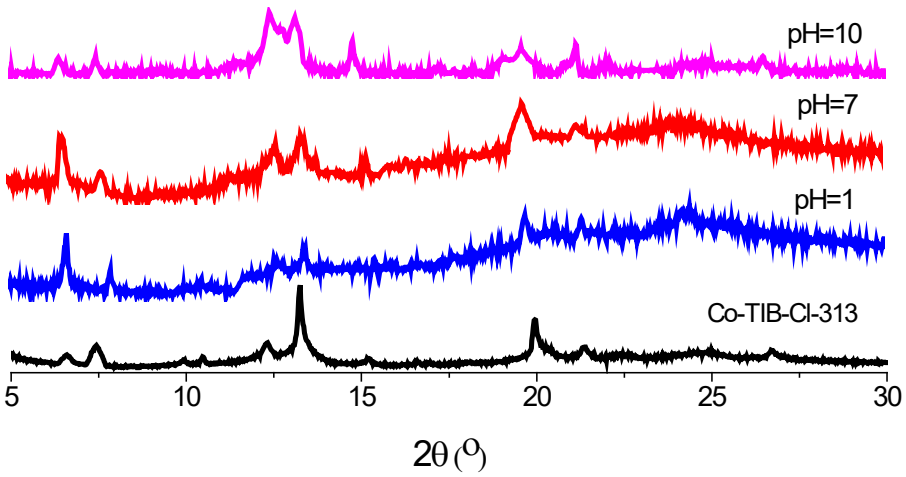

Fig. S28 The stability of **Co-TIB-NO$_3$-313** in water with various pH values. In contrast to the PXRD pattern in the crystalline CP from of Co-TIP-Cl-313, it is clear that formation of crystalline CP from was observed, when soaking **Co-TIB-NO$_3$-313** in water with pH=1, 7, and 10.

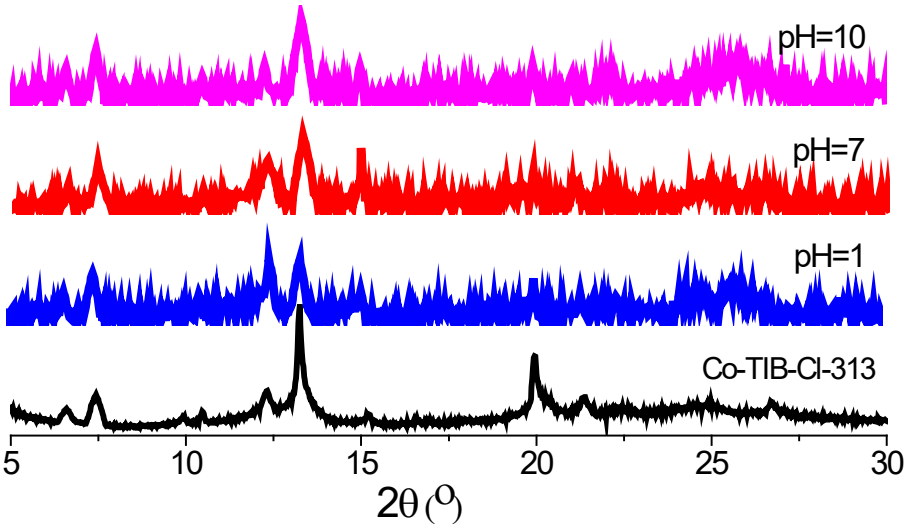

Fig. S29 The stability of **Co-TIB-Cl-313** in water with various pH values. In contrast to the PXRD pattern in the crystalline CP from of Co-TIP-Cl-313, it is clear that maintenance of crystalline CP from was observed, when soaking **Co-TIB-Cl-313** in water with pH=1, 7, and 10.

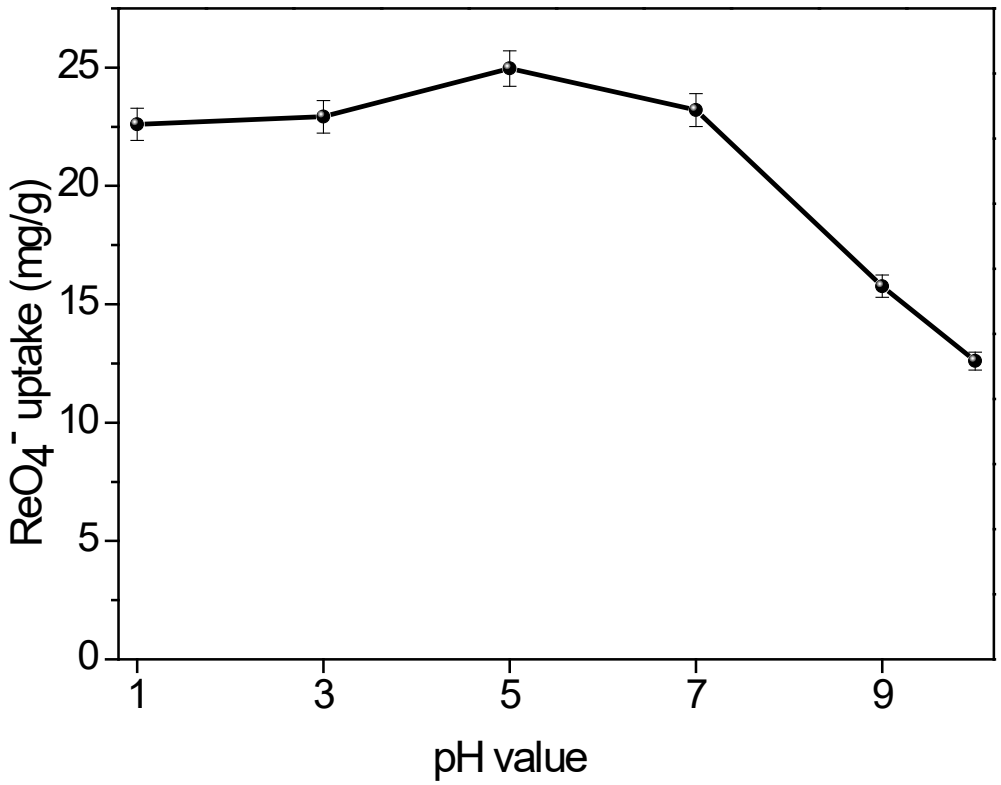

Fig. S30 View of the ReO_4^- uptake for **Co-TIB-NO3-313** under pH=1-10 (C_0=15 ppm, m=10 mg, V=20 mL, T=298 K, Time=5 h). HNO_3 (1 M) and NaOH (1 M) was used to adjust pH value.

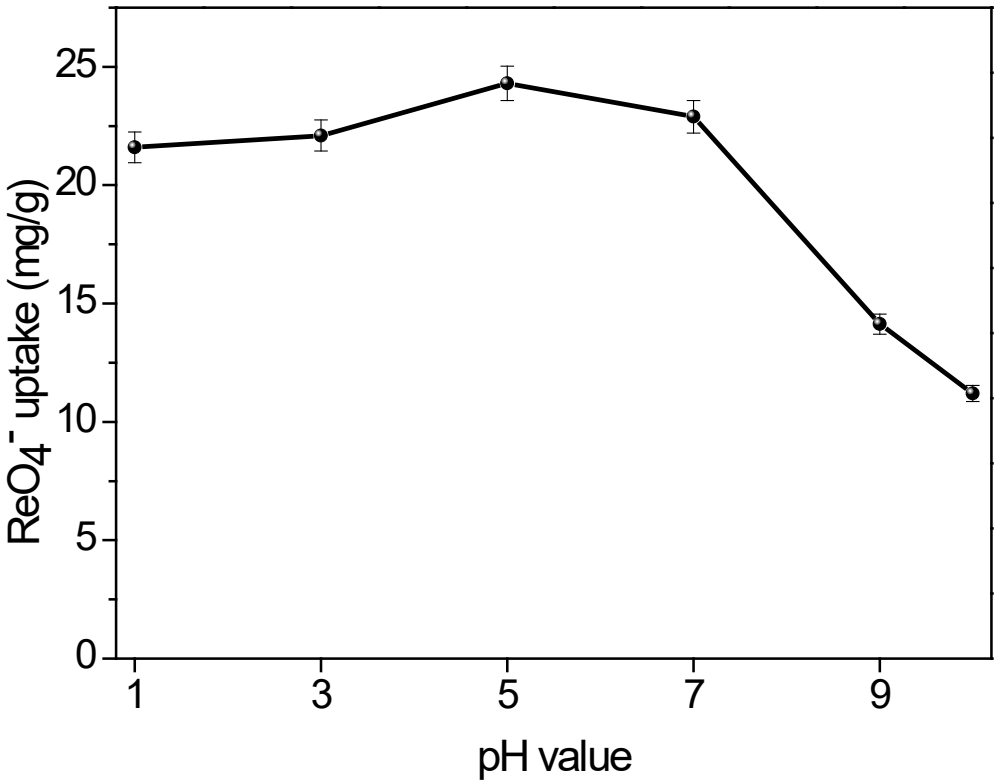

Fig. S31 View of the ReO_4^- uptake for **Co-TIB-Cl-313** under pH=1-10 (C_0=15 ppm, m=10 mg, V=20 mL, T=298 K, Time=5 h). HNO_3 (1 M) and NaOH (1 M) was used to adjust pH value.

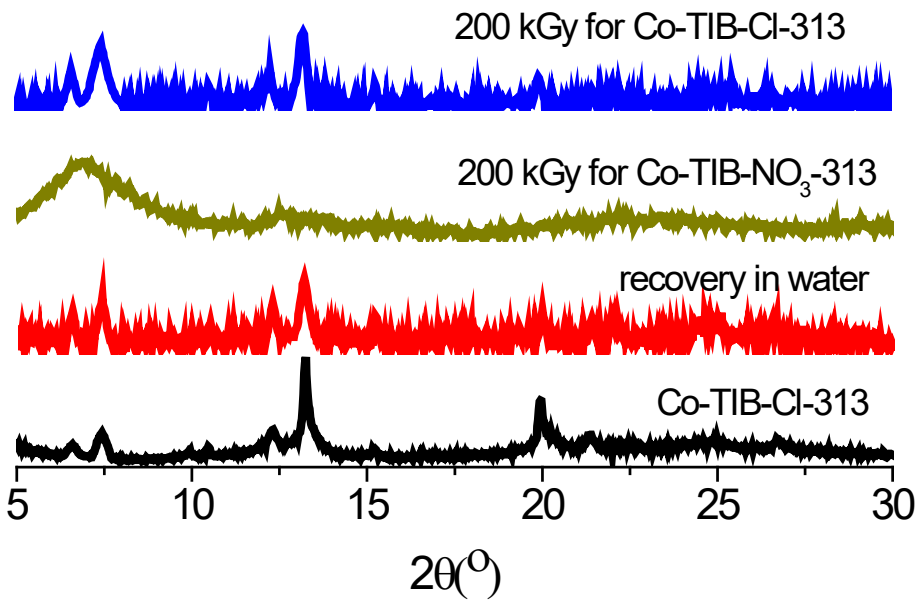

Fig. S32 PXRD patterns were used to trace the stability of these samples after β-irradiation at a dose rate of 20 kGy/h for 10 h. For samples of **Co-TIB-NO$_3$-313**, to confirm the maintenance of the integrity of the framework, the recovery to crystalline CP phase (as observed in **Co-TIB-NO$_3$-313**) was observed, when soaking corresponding samples in water.

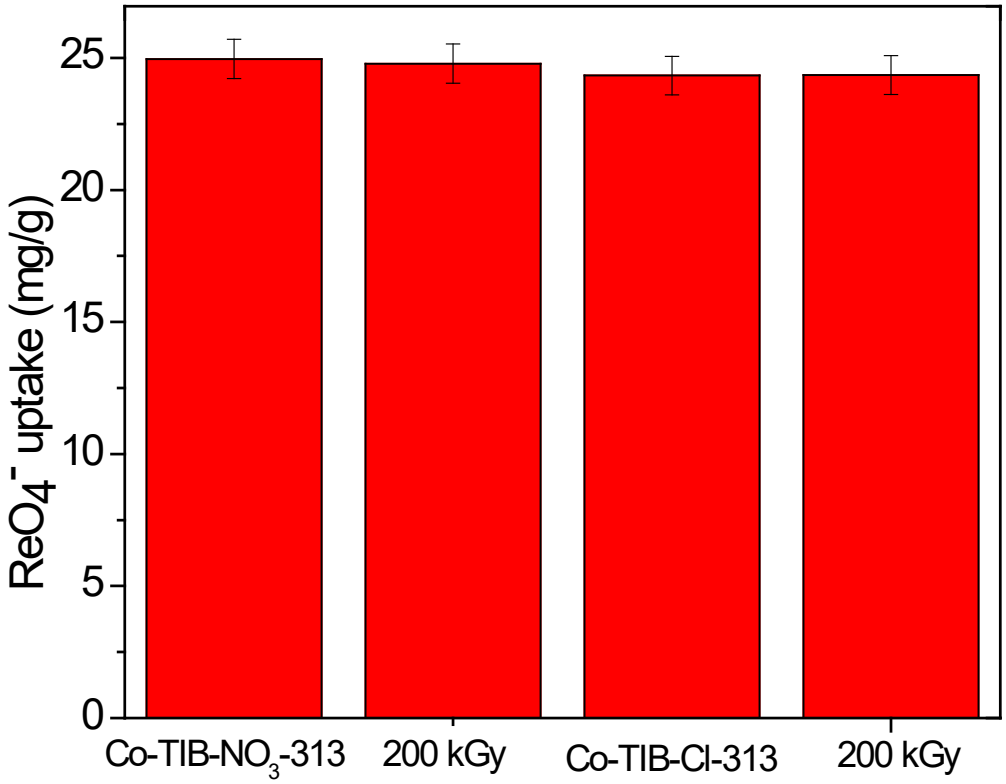

Fig. S33 A comparison of ReO_4^- uptake for the samples of **Co-TIB-NO3-313** and **Co-TIB-Cl-313** before and after β-Irradiation (C_0=18 ppm, m=10 mg, V=20 mL, T=298 K, Time=5 h).

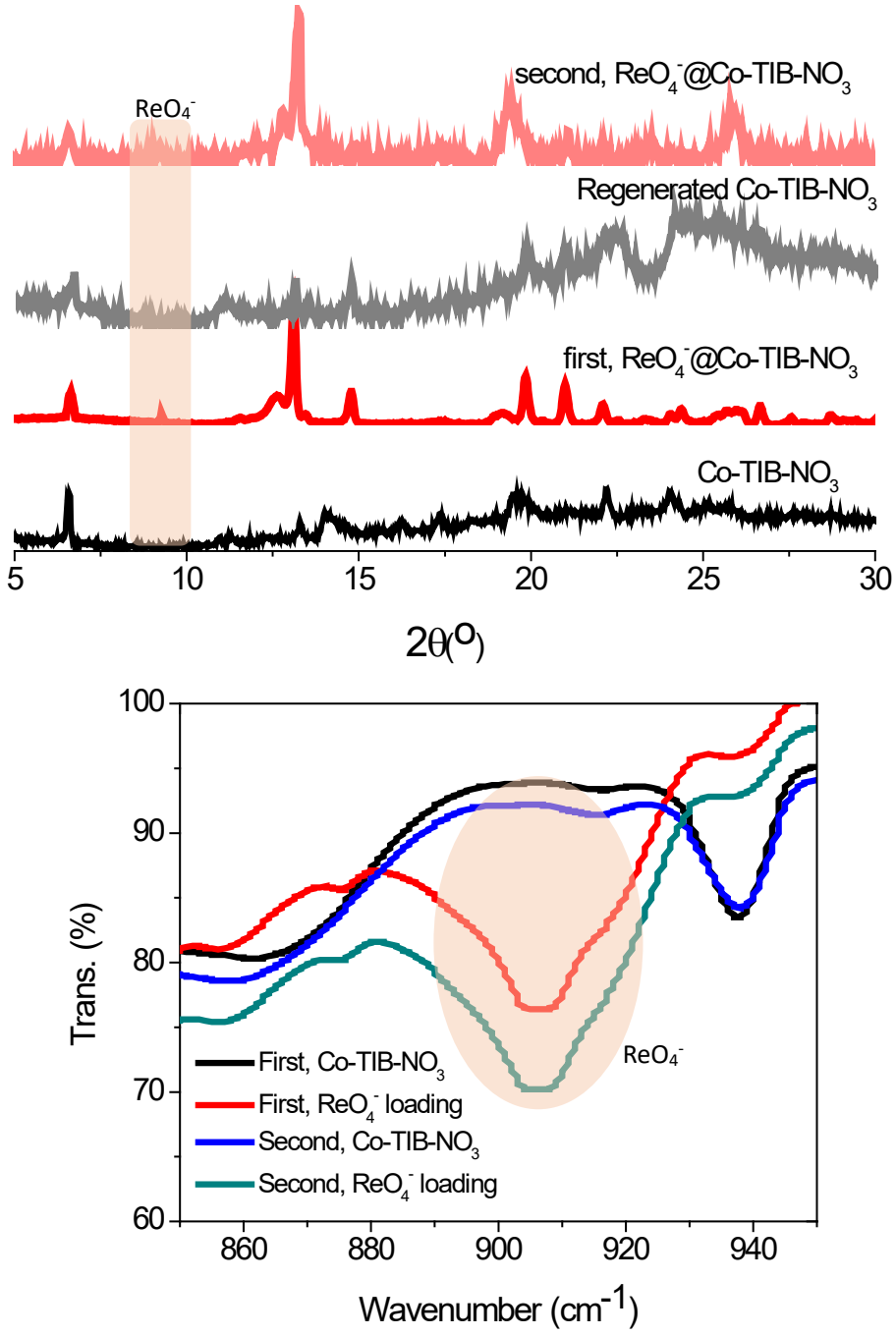

Fig. S34 A comparison of PXRD patterns and IR among the samples of **Co-TIB-NO3** and its ReO_4^- loading counterpart. Two cycles was explored, where it is clear that the PXRD peak at 9.33 is due to ReO_4^- loading.

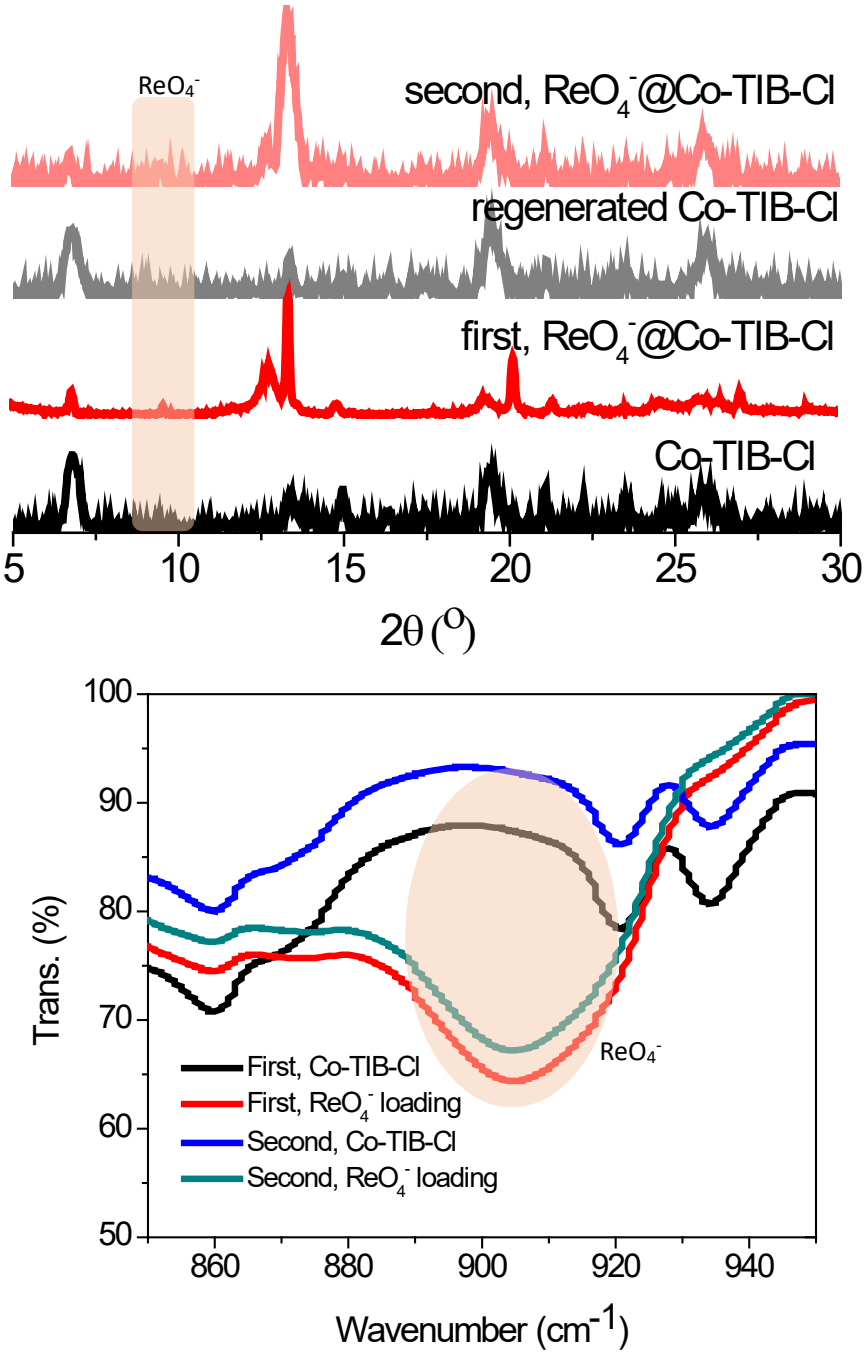

Fig. S35 A comparison of PXRD patterns and IR among the samples of **Co-TIB-Cl** and its ReO_4^- loading counterpart. Two cycles was explored, where it is clear that the PXRD peak at 9.43 is due to ReO_4^- loading.

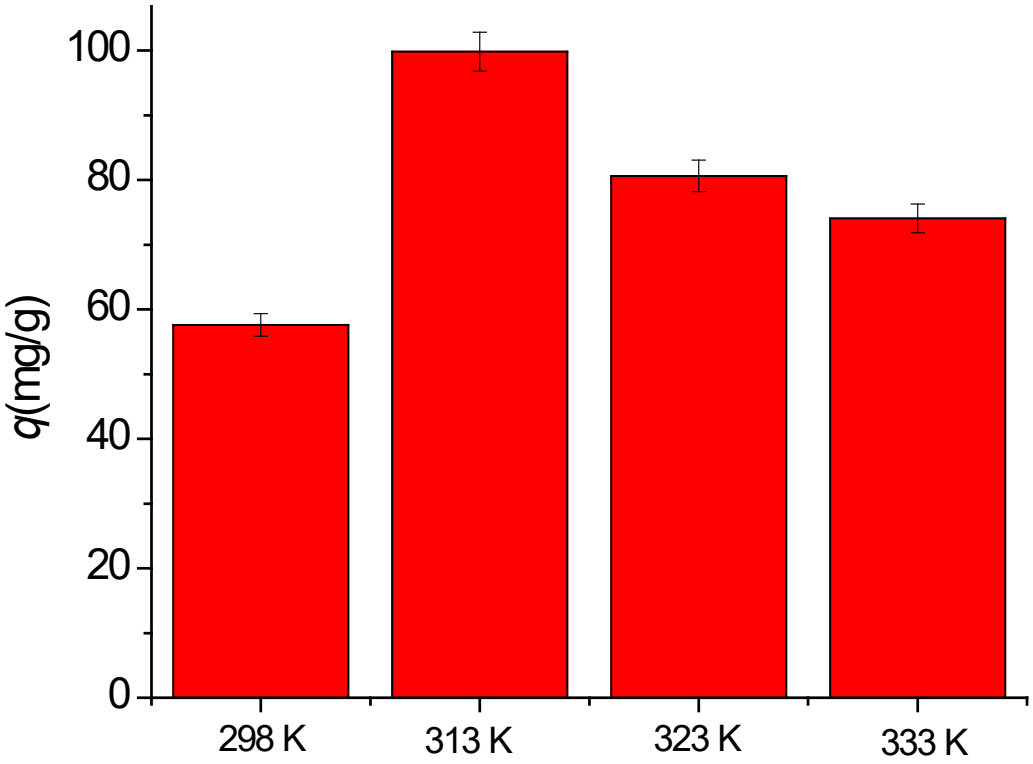

Fig. S36 A comparison of ReO_4^- uptake for NO_3^--containing samples generated at various temperature (C_0=53 ppm, m=10 mg, V=20 mL, T=298 K, Time=5 h).

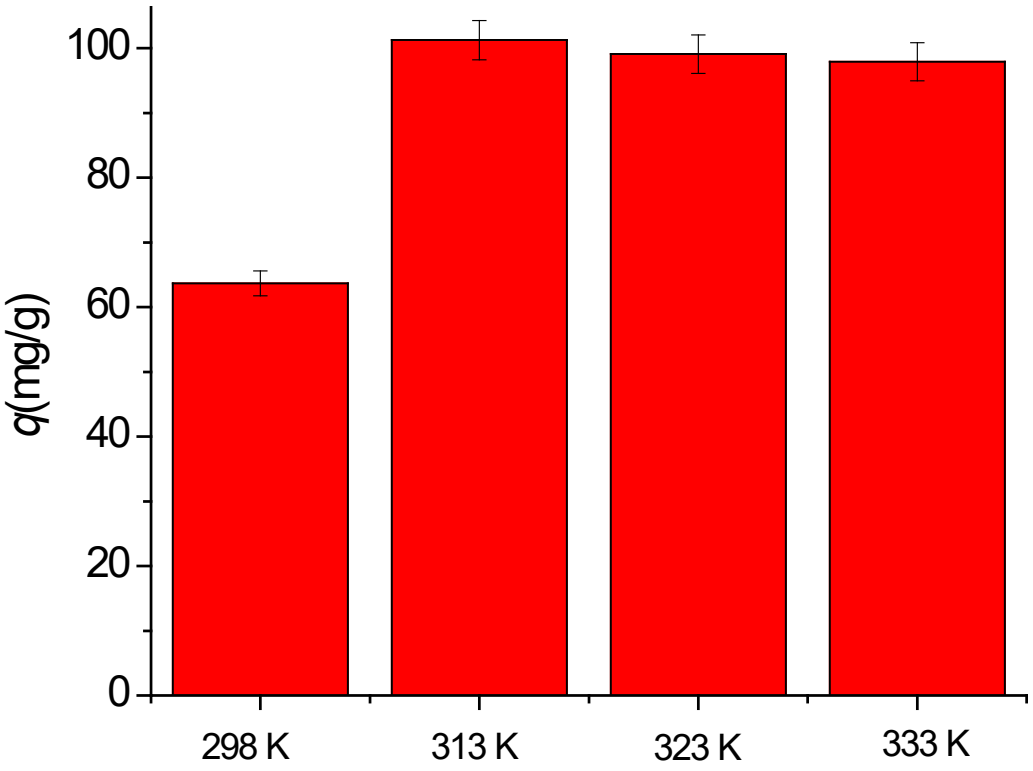

Fig. S37 A comparison of ReO_4^- uptake for Cl^--containing samples generated at various temperature (C_0=53 ppm, m=10 mg, V=20 mL, T=298 K, Time=5 h).

Table S1. A summary of the crystallographic parameters involved in this work.

Compounds	Co-TIB-NO_3	Co-TIB-NO_3-308	Co-TIB-NO_3-R	Co-TIB-Cl	Co-TIB-Cl-313	Co-TIB-Cl-R
Temperature(K)	298(2)	308(2)	240(10)	298(2)	313(2)	298(2)
Crystal system	Tetragonal	Tetragonal	Tetragonal	Tetragonal	Tetragonal	Tetragonal
Space group	I4/mcm	I4/mcm	I4/mcm	I4/mcm	I4/mcm	I4/mcm
Unit cell dimensions (Å)	18.2441(10)	18.1936(6)	18.1772(10)	18.2181(3)	16.497(2)	18.2729(10)
	18.2441(10)	18.1936(6)	18.1772(10)	18.2181(3)	16.497(2)	18.2729(10)
	26.915(4)	26.897(2)	26.738(2)	26.3120(9)	26.594(6)	26.293(4)
Volume ($Å^3$)	8958.6(15)	8903.3(8)	8834.5(12)	8732.9(4)	7238(2)	8779.3(14)
R indices (all data)	R1=0.1225	R1=0.1773	R1=0.0705	R1=0.1189	R1=0.1882	R1=0.1218
	wR_2= 0.2233	wR_2=0.3032	wR_2= 0.1960	wR_2=0.3433	wR_2=0.3404	wR_2=0.2638
CCDC number	2201231	2201226	2201228	2201230	2201227	2201229

For Cl-replaced samples (generated 323 K, and 333 K), the recovery to crystalline OP form was confirmed by the determination of unit cell, giving a=b=18.1648(9), c=26.274 (3) for 323 K and a=b=18.3317 (10), c=26.165 (4) for 333 K.

Table S2. Kinetic parameters of pseudo-first-order and pseudo-second-order models.

Adsorbent	$q_{e,\exp}$ (mg·g^{-1})	pseudo-first-order			pseudo-second-order		
		$q_{e,cal}$ (mg·g^{-1})	k_1 (min^{-1})	R^2	$q_{e,cal}$ (mg·g^{-1})	k_2 (g·mg^{-1}·min^{-1})	R^2
Co-TIB-NO_3	146.41	122.067	0.0664	0.8550	156.006	0.00038	0.9967
Co-TIB-Cl	152.54	79.815	0.0489	0.9114	156.740	0.00082	0.9999
Co-TIB-NO_3-313	186.36	138.951	0.0737	0.9602	196.078	0.00044	0.9989
Co-TIB-Cl-313	188.51	113.750	0.0422	0.9376	194.932	0.00048	0.9994

Table S3. Isotherm parameters of Langmuir and Freundlich models.

Adsorbent	Langmuir model				Freundlich model		
	$q_{e,\exp}$ (mg·g^{-1})	K_L (L·mg^{-1})	q_m (mg·g^{-1})	R^2	K_F (mg$^{1-1/n}$·g^{-1}·L$^{-1/n}$)	$1/n$	R^2
Co-TIB-NO_3	284.18	0.0113	348.432	0.9858	24.403	0.4199	0.8883

Co-TIB-Cl	391.71	0.0250	427.350	0.9931	98.727	0.2319	0.9836
Co-TIB-NO_3-313	539.55	0.0206	613.497	0.9958	71.243	0.3571	0.9523
Co-TIB-Cl-313	460.77	0.0182	507.614	0.9934	78.038	0.2968	0.9758

Table S4. A comparison table of ReO_4^- capture with some well-studied examples in the literature.

	Compounds	Uptake capacity (mg/g)	Reference
MOFs	UIO-66-NH_3^+Cl	159	Inorg. Chem. 2016, 55, 8241-8243
	NU-1000	210	Chem. Mater. 2018, 30, 1277-1284
	SCU-101	217	J. Am. Chem. Soc. 2017, 139, 14873-14876
	SCU-103	318	Nat. Commun. 2020, 11, 5571
	Co-TIB-NO_3	281	Our work
	Co-TIB-Cl	392.9	Our work
	Co-TIB-Cl-313	459.6	Our work
	Co-TIB-NO_3-313	540	Our work
	SCU-100	553	Environ. Sci. Technol. 2017, 51, 3471-3479
	Th-MOF-68	560	Nano. Res. 2022, 15, 1472-1478
	SLUG-21	602	J. Am. Chem. Soc. 2010, 132, 7202-7209
	iMOF-2C	691	ACS Appl. Mater. Inter. 2020, 12, 41810-41818
	CAU-1	692	J. Hazard. Mater. 2021, 407, 5, 124729
	SBN	786	Environ. Sci. Technol. Lett. 2017, 4, 316-322
	Th-MOF	807	Angew. Chem. Int. Ed. 2019, 131, 6083-6088
	MOR-2	1025	J. Mater. Chem. A, 2018, 6, 20813-20821
Inorganic compounds	MgAl-LDHs	112	Water Res. 2009, 43, 3067-3075
	$YPbOClO_4$-1	434	Adv. Sci. 2019, 6, 1900381
Polymer	PAF-1-F	420	Chem. Eur. J. 2016, 22, 17581-17584
	SCU-CPN-1	999	Nat. Commun. 2018, 9, 3007
	PQA-pN$(Me)_2$Py-Cl	1127	Nat Commun. 2019, 10, 1646
	SCU-CPN-2	1467	Sci. China Chem. 2021, 64, 1251-1260
COFs	PS-COF-1	1262	Sci. Bull. 2022, 67, 924-932
	NKCOF-41-Cl^-	1078	Angew. Chem. Int. Ed. 2022, 61, e202213247